Nano Research
2019, 12(7): 1713–1719

ISSN 1998-0124 CN 11-5974/O4
https://doi.org/10.1007/s12274-019-2427-3

Research Article

High-performance Li-ion capacitor based on black-TiO_{2-x}/graphene aerogel anode and biomass-derived microporous carbon cathode

Guoyin Zhu[1,§], Lianbo Ma[1,§], Huinan Lin[1,§], Peiyang Zhao[1], Lei Wang[1], Yi Hu[1], Renpeng Chen[1], Tao Chen[1], Yanrong Wang[1], Zuoxiu Tie[1] (✉), and Zhong Jin[1,2] (✉)

[1] *Key Laboratory of Mesoscopic Chemistry of MOE, Jiangsu Key Laboratory of Advanced Organic Materials, School of Chemistry and Chemical Engineering, Nanjing University, Nanjing 210023, China*
[2] *Shenzhen Research Institute of Nanjing University, Shenzhen 518063, China*
[§] *Guoyin Zhu, Lianbo Ma, and Huinan Lin contributed equally to this work.*

Received: 23 December 2018 / **Revised:** 9 April 2019 / **Accepted:** 29 April 2019

ABSTRACT

Lithium-ion capacitor (LIC) has been regarded as a promising energy storage system with high powder density and high energy density. However, the kinetic mismatch between the anode and the cathode is a major issue to be solved. Here we report a high-performance asymmetric LIC based on oxygen-deficient black-TiO_{2-x}/graphene (B-TiO_{2-x}/G) aerogel anode and biomass derived microporous carbon cathode. Through a facile one-pot hydrothermal process, graphene nanosheets and oxygen-vacancy-rich porous B-TiO_{2-x} nanosheets were self-assembled into three-dimensional (3D) interconnected B-TiO_{2-x}/G aerogel. Owing to the rich active sites, high conductivity and fast kinetics, the B-TiO_{2-x}/G aerogel exhibits remarkable reversible capacity, high rate capability and long cycle life when used as anode material for lithium ion storage. Moreover, density functional theory (DFT) calculation reveals that the incorporation of graphene nanosheets can reduce the energy barrier of Li^+ diffusion in B-TiO_{2-x}. The asymmetric LIC based on B-TiO_{2-x}/G aerogel anode and naturally-abundant pine-needles derived microporous carbon (MPC) cathode work well within a large voltage window (1.0–4.0 V), and can deliver high energy density (166.4 $Wh\cdot kg^{-1}$ at 200 $mA\cdot g^{-1}$), and high power density (7.9 $kW\cdot kg^{-1}$ at 17.1 $Wh\cdot kg^{-1}$). Moreover, the LIC shows a high capacitance retention of 87% after 3,000 cycles at 2,000 $mA\cdot g^{-1}$. The outstanding electrochemical performances indicate that the rationally-designed LICs have promising prospect to serve as advanced fast-charging energy storage devices.

KEYWORDS

lithium-ion capacitors, oxygen-deficient B-TiO_{2-x}/graphene aerogel anode, biomass-derived microporous carbon, high energy density

1 Introduction

As the "second generation" supercapacitors, lithium-ion capacitors (LICs) have been considered as one of the most promising hybrid energy storage devices combining the high power density of electrochemical double-layer capacitors (EDLCs) and the high energy density of lithium-ion batteries (LIBs) [1]. The overall reaction process of hybrid LICs integrates the reversible Li^+ adsorption/desorption on one electrode and the reversible Li^+ insertion/extraction reaction in another electrode [2–4]. The LICs are considered to meet the high-energy and high-power demands for different applications, ranging from wearable electronic devices to smart grid energy technologies [5–7]. However, a key issue is the kinetic imbalance between the capacitor-type cathode and the battery-type anode, because the reaction kinetics of battery-type anode materials for Li^+ intercalation is usually slow [8]. On the other hand, the specific capacity of capacitor-type cathode is not high, which limites the overall capacity of LICs [9]. Thus, the optimization of cathode and anode materials, in particular, the development of high-rate anodes, remains challenging for improving the overall performance of LICs.

To realize the kinetics balance of LICs, suitable anode materials with fast Li^+ insertion/extraction reaction kinetics show great promise. Many metal oxides such as Fe_3O_4 [10, 11], MnO [12, 13], TiO_2 [14, 15], Nb_2O_5 [16, 17], and MoO_3 [18, 19] have been studied as potential anode materials for LICs because of the high theoretical capacity (500–1,000 $mAh\cdot g^{-1}$) and relatively low-voltage plateau (about 0.8 V). Among the metal oxides-based anode materials, TiO_2 has been explored as a potential anode material owing to its environmental-friendliness, low cost, and stable cycling performance with safety features [20]. Nevertheless, its intrinsic poor conductivity and slow Li^+ diffusion may lead to poor rate capability and cycling lifetime, thus seriously restricting the practical application [21]. In order to improve the electrical transport properties of TiO_2, an effective strategy is to narrow the band gap of TiO_2 by defect engineering or heteroatom doping [22]. In this regard, oxygen-deficient TiO_{2-x} containing Ti^{3+} species with narrowed band gap can provide greatly enhanced conductivity, hence it has been regarded as a promising anode material in sodium-ion batteries [23]. Additionally, another effective strategy to improve the electrical conductivity is the introduction of conductive carbon materials [24, 25]. Among the carbonaceous materials, graphene nanosheets are promising due to good conductivity and high specific surface area that can provide abundant active sites. Activated carbon has been widely used as a common cathode material in LICs, owing to the large surface area, but its specific capacity is low (30–35 $mAh\cdot g^{-1}$). In our previous work, heteroatom-doped microporous carbon (MPC) derived from pine

---

Address correspondence to Zuoxiu Tie, zxtie@nju.edu.cn; Zhong Jin, zhongjin@nju.edu.cn

needles show high surface area and excellent rate capacity [26], which is suitble to be used as an improved cathode material for LICs.

Following this line of thought, here we propose the design of hybrid LICs based on oxygen-deficient black TiO_{2-x}/graphene (B-TiO_{2-x}/G) aerogel as battery-type anodes and pine needles-derived microporous carbon as capacitor-type cathodes. Through a facile one-step hydrothermal approach, B-TiO_{2-x}/G aerogel with outstanding structural and compositional characteristics was synthesized. The oxygen-vacancy-rich porous B-TiO_{2-x} nanosheets show greatly improved conductivity and diffusion kinetics for Li^+ storage. Moreover, the three-dimensional (3D) hierarchical porous structure of B-TiO_{2-x}/G aerogel combining the B-TiO_{2-x} and graphene nanosheets provides abundant active sites and short ion diffusion pathways. Moreover, first-principles calculation reveals that the introduction of graphene nanosheets can reduce the energy barrier of Li^+ diffusion, which can further enhance the electrochemical performance of B-TiO_{2-x}/G aerogel. Thus, the B-TiO_{2-x}/G aerogel can be employed as an advanced anode material for hybrid LICs. By coupling the 3D B-TiO_{2-x}/G aerogel anode with biomass-derived MPC cathode, we successfully fabricated high-performance LICs with wide operating voltage window (1.0–4.0 V), long cycle life (~ 87% capacity retention after 3,000 cycles), high energy density (166.4 $Wh·kg^{-1}$ at 200 $mA·g^{-1}$), and high power output (7.9 $kW·kg^{-1}$ at 5,000 $mA·g^{-1}$), which are very remarkable among the existing LICs (Table S1 in the Electronic Supplementary Material (ESM)) [5, 15, 16, 27–38]. This study provides an efficient approach to improve the electrochemical performance of LICs via the synergistic combination of oxygen vacancies and conductive carbon matrix.

2 Experimental details

2.1 Synthesis of oxygen-deficient black TiO_{2-x} (B-TiO_{2-x}) nanosheets

In a typical synthesis [39], 10 mL of tetrabutyl titanate ($TiOBu_4$, Sigma Aldrich) was mixed with 1.5 mL of hydrofluoric acid (HF, 40.0 wt.%, Arcos Organics) under vigorous stirring for 3 h. Then, the solution was transferred into a Teflon-lined autoclave and heated in an oven at 180 °C for 24 h. After the reaction, the solid material was collected by ultracentrifugation at a speed of 6,000 rpm for 10 min. Finally, the suspension was dried under vacuum at 60 °C. The powder was then collected and annealed at 600 °C in Ar/H_2 (95% Ar and 5% H_2) atmosphere for 3 h.

2.2 Synthesis of B-TiO_{2-x}/G aerogel

Graphene oxide (GO) was prepared from graphite powder by a modified Hummer's method. In a typical synthesis, 30 mg of GO was dispersed into 30 mL of deionized (DI) water under sonication for 3 h. Then, 6 mg as-synthesized B-TiO_{2-x} nanosheets were added into the homogeneous GO suspension and stirred for 1 h. The resulting mixture was transferred into a 50 mL Teflon-lined autoclave and was maintained at 180 °C for 12 h. After natural cooling in room temperature, a black monolithic cylinder of B-TiO_{2-x}/G aerogel was obtained. The resultant product was rapidly frozen in liquid nitrogen and then freeze-dried in vacuum at −25 °C for 48 h for the following experiment.

2.3 Synthesis of pine needles-derived MPC

The biomass derived activated carbon was synthesized as described in our previous work [26]. Briefly, the pine needles were pre-carbonized at 600 °C for 60 min under an N_2 atmosphere. The pre-carbonized samples were then mixed with KOH ($weight_{KOH}/weight_{carbon} = 4$), and calcined at 900 °C for 1 h under a N_2 flow of 50 sccm and a heating rate of 5 °C/min. Then the collected dark powder was washed with excess HCl solution (10 wt.%) and distilled water, and finally dried at 120 °C overnight.

2.4 Materials characterizations

The prepared samples were examined by transmission electron microscopy (TEM, JEM-2100). Scanning electron microscopy (SEM) and energy dispersive X-ray spectroscopy (EDS) elemental mapping were performed on a FET Nova NanoSEM 450 instrument. X-ray power diffraction (XRD) patterns were measured on a Shimadzu XRD-600 diffractometer with Cu Kα radiation (λ = 1.5418 Å). X-ray photoelectron spectroscopy (XPS) spectra were measured on PHI-5000 VersaProbe X-ray photoelectron spectrometer with an Al Kα X-ray radiation. Nitrogen adsorption–desorption isotherms were recorded using Quantachrome Autosorb-IQ-2C-TCD-VP analyzer, and Raman spectroscopy was performed using a Horiba JY Evolution Raman spectrometer with an excitation laser of 633 nm wavelength.

2.5 Electrochemical characterizations

The electrochemical analysis of the B-TiO_{2-x}/G aerogel half-cells, MPC half-cells and B-TiO_{2-x}/G aerogel||MPC LICs were conducted. The electrodes were prepared by blade-coating the slurries of active materials, conductive carbon black, and polyvinylidene fluoride (PVDF) in a weight ratio of 8:1:1 mixed with N-methyl pyrrolidone (NMP) on metal foils, and dried at 100 °C for 12 h. The B-TiO_{2-x}/G aerogel||Li and Li||MPC half-cells were assembled in an Ar-filled glovebox by using Li-metal foils as counter electrodes. The working electrodes and Li foils were separated by Celgard 2400 membranes with a 1.0 M $LiPF_6$ solution of ethylene carbonate (EC) and dimethyl carbonate (DEC) (1:1 by volume) as electrolyte. The LICs were assembled as two-electrode cells using the prelithiated B-TiO_{2-x}/G aerogel anodes and the MPC cathodes. The optimized mass ratio of active materials for the cathode and anode was ~ 8:1. Cyclic voltammetry (CV) was examined by a VMP3 Electrochemical Workstation (Bio-logic) analyzer. The charge–discharge tests were measured by a LAND CT2001A battery measurement system. All the electrochemical tests were performed at room temperature.

The single electrode discharge capacitances (C_s) were obtained from the discharging curves according to the following equation

$$C_s = 4 \times I \times \Delta t / m \times (V_f - V_i) \qquad (1)$$

The specific energy density and power density were calculated by the following equations

$$P = \Delta V \times I / m \qquad (2)$$

$$E = P \times t / 3600 \qquad (3)$$

$$\Delta V = (V_f + V_i) / 2 \qquad (4)$$

where V_f and V_i are the potential ranges, I (A) is the discharging current, m (g) is the mass of the active material, P ($W·kg^{-1}$) is the power density, and E ($Wh·kg^{-1}$) is the energy density.

2.6 Density functional theory (DFT) calculations

The theoretical calculations were performed using Vienna *ab-initio* simulation package (VASP) [40–43]. The generalized gradient approximation of the Perdew–Burke–Ernzerhof (GGA-PBE) was used to describe the exchange-correlation functional [44]. The wave functions at each k-point were expanded with a plane wave basis set and a kinetic cutoff energy up to 400 eV. Brillouin zone integration was approximated by a sum over special selected k-points using the 1 × 3 × 1 Monkhorst–Pack sampling [45]. Atomic geometries were optimized until the energy was converged to 1.0×10^{-6} $eV·atom^{-1}$ and the force was converged to 0.01 $eV·Å^{-1}$, respectively. During the geometry optimizations, the bottom layer atoms were fixed in their bulk positions, while the other atomic layers and the covered graphene layer were allowed to relax. A vacuum layer as large as 15 Å between repeated slabs was used along the c direction to avoid periodic interactions.

In order to minimize the lattice mismatch effects between the TiO_2 lattice and the covered graphene, we have constructed the interface structure of graphene and $TiO_2(101)$ surface with 11 × 3 supercell and 5 × 2 supercell, respectively. The $TiO_2(101)$ surface is selected because it is one of the most exposed facets in the TiO_2/G composites. The $TiO_2(101)$/graphene composite contains 40 titanium atoms, 80 oxygen atoms and 66 carbon atoms, respectively. Considering the influence of weak van der Waals (vdW) interaction, we employed a semiempirical DFT-D2 force-field approach [46, 47] to describe the interlayer interaction in the $TiO_2(101)$/graphene system.

To evaluate the stability of $TiO_2(101)$/graphene structure, we have calculated the formation energy of graphene on the $TiO_2(101)$ surface, which was defined as follows

$$E_{\text{formation}} = E_{\text{TiO}_2\,(101)/\text{graphene}} - E_{\text{TiO}_2\,(101)} - E_{\text{graphene}} \tag{5}$$

where $E_{\text{TiO}_2\,(101)/\text{graphene}}$, $E_{\text{TiO}_2\,(101)}$ and E_{graphene} are the energies of the composite $TiO_2(101)$/graphene structure, the isolated $TiO_2(101)$, and the isolated graphene, respectively. The formation energy for graphene on the $TiO_2(101)$ surface is calculated to be −10.73 eV, indicating the $TiO_2(101)$/graphene hybrid structure is very stable.

The adsorption energies (ΔE_{ads}) of Li atom on the isolated $TiO_2(101)$ or the $TiO_2(101)$/graphene composite were defined as follows

$$\Delta E_{\text{ads}} = E_{\text{Li}/\text{slab}} - E_{\text{slab}} - \mu_{\text{Li}} \tag{6}$$

where $E_{\text{Li}/\text{slab}}$ is the total energy of Li atom on the isolated $TiO_2(101)$ or the $TiO_2(101)$/graphene composite, E_{slab} is the total energy of the isolated $TiO_2(101)$ or the $TiO_2(101)$/graphene composite, and μ_{Li} is the chemical potential of lithium atom defined as the total energy per lithium atom in bulk phase lithium.

3 Results and discussion

The schematic preparation process of B-TiO_{2-x}/G aerogel is presented in Fig. 1 and detailed in the Experimental Section. Briefly, well-defined oxygen-deficient B-TiO_{2-x} nanosheets were firstly prepared via solution-phase hydrolysis and subsequent Ar/H_2 thermal annealing. The B-TiO_{2-x} nanosheets were hydrothermally treated together with GO prepared by Hummers method [48], and then followed by freeze-drying to get the desired B-TiO_{2-x}/G aerogel. During the hydrothermal treatment, GO nanosheets were reduced into graphene nanosheets and self-assembled with B-TiO_{2-x} nanosheets to form a 3D interconnected aerogel network due to π–π stacking interactions. The digital photograph in Fig. 1 displays the shape and dimension of as-prepared monolithic B-TiO_{2-x}/G aerogel with black color, comprised of homogenously assembled graphene and B-TiO_{2-x} nanosheets.

Figures 2(a)–2(d) depict the morphologic features of as-prepared B-TiO_{2-x}/G aerogel. SEM images (Figs. 2(a) and 2(b)) display the porous and 3D interconnected structure of B-TiO_{2-x}/G aerogel. It can be seen that the wrinkled and porous walls of B-TiO_{2-x}/G composite are made up of loosely-interlinked graphene sheets, where B-TiO_{2-x} nanosheets are uniformly anchored on the surface of graphene nanosheets. TEM images (Figs. 2(c) and 2(d)) reveal the layer structure and ultrathin thickness of graphene and B-TiO_{2-x} nanosheets. High-resolution TEM (HRTEM) image of B-TiO_{2-x} nanosheets shows a crystalline lattice spacing of 0.35 nm (Fig. 2(d)), corresponding to the (101) lattice planes of anatase phase B-TiO_{2-x} [49, 50]. Figure 2(e) shows a high-angle annular dark-field scanning TEM (HAADF-STEM) image and corresponding energy dispersive X-ray spectroscopy (EDX) elemental mappings of B-TiO_{2-x}/G aerogel, showing the presence and homogenous spatial distribution of Ti, C, and O elements in the porous framework of B-TiO_{2-x}/G aerogel.

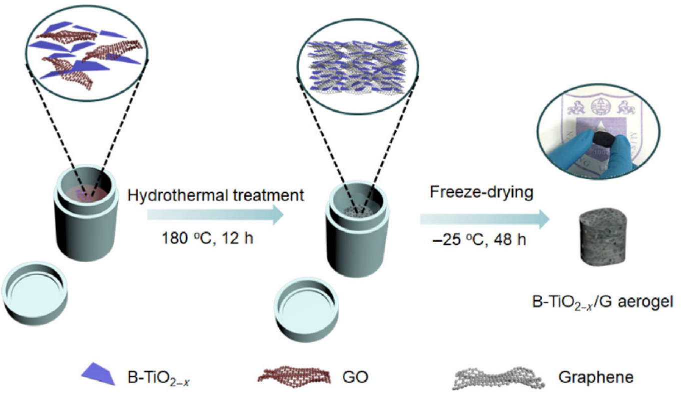

Figure 1 Schematic synthetic procedures of 3D interconnected B-TiO_{2-x}/G aerogel.

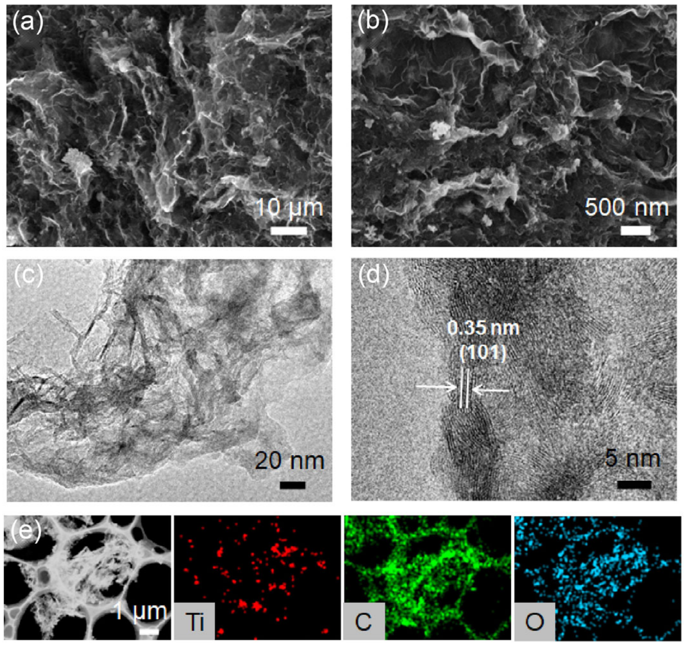

Figure 2 (a) and (b) SEM and (c) and (d) TEM images of B-TiO_{2-x}/G aerogel. (e) HAADF-STEM image and corresponding elemental mappings of B-TiO_{2-x}/G aerogel.

The XRD patterns of pristine B-TiO_{2-x} nanosheets and B-TiO_{2-x}/G aerogel are shown in Fig. 3(a), both matching with anatase phase TiO_2 (JCPDS card No. 21-1272) [20]. In the case of the B-TiO_{2-x}/G aerogel, a broad peak between 15°–35° is identified to be the (002) plane of stacked graphene nanosheets, which also suggests the loss of long-range order in graphene [51]. Figure 3(b) shows the survey XPS spectrum of B-TiO_{2-x}/G aerogel, in which C 1s, Ti 2p, and O 1s bands are observed. The C 1s XPS spectrum (Fig. 3(c)) shows two main peaks associated with C–C (284.6 eV) and C=C (285.3 eV), and three weak peaks derived from C–O (286.3 eV), C=O (287.4 eV) and O–C=O (289.9 eV) [52]. The results indicate that most of oxygen-containing functional groups were removed during the hydrothermal treatment. The chemical states of Ti species of B-TiO_{2-x}/G aerogel were clarified by Ti 2p XPS spectrum (Fig. 3(d)). The two peaks at 459.3 and 456.0 eV were ascribed to Ti^{4+} and Ti^{3+}, respectively. The atomic ratio of Ti^{3+}:Ti^{4+} was calculated to be 12.2:87.8, thus the proportion of Ti and O in the B-TiO_{2-x} can be estimated to be $TiO_{1.94}$. The presence of electroconducting Ti^{3+} could change the structure of TiO_2 and convert the white color to black, in accordance with previous literature [22]. Furthermore, self-doped Ti^{3+} species in the crystalline structure can narrow the wide band gap to a semiconductor level, providing good electrical conductivity and resulting in the electrochemical performance improvement of

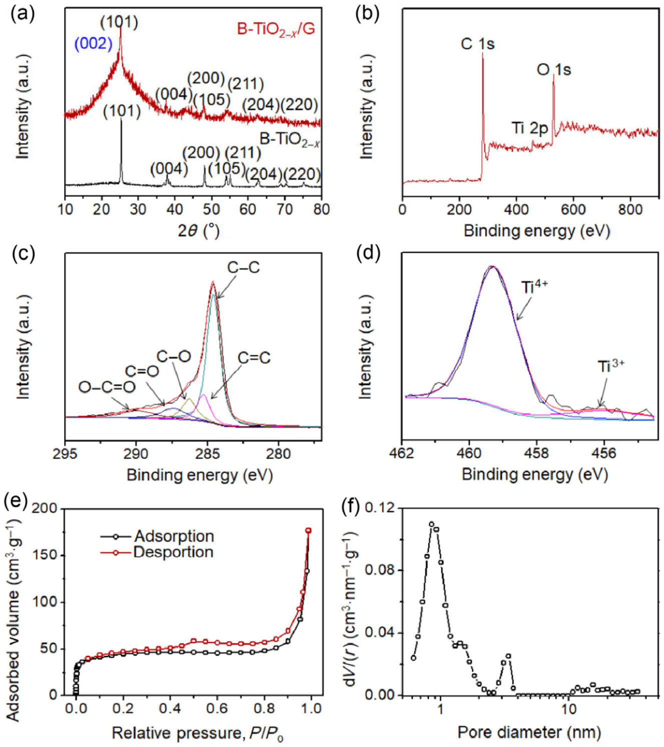

Figure 3 (a) XRD patterns of B-TiO_{2-x} nanosheets and B-TiO_{2-x}/G aerogel. (b) XPS spectrum of B-TiO_{2-x}/G aerogel. (c) and (d) High-resolution XPS spectra at (c) C 1s and (d) Ti 2p energy levels of B-TiO_{2-x}/G aerogel. (e) Nitrogen sorption isotherms and (f) pore size distribution of B-TiO_{2-x}/G aerogel.

B-TiO_{2-x}/G aerogel [53]. The structural information was further investigated by Raman spectroscopy (Fig. S1 in the ESM). Four characteristic peaks at 153, 394, 506 and 627 cm^{-1} were assigned to the E_g, B_{1g}, A_{1g} and E_g bands of B-TiO_{2-x}. The other two Raman peaks at 1,330 and 1,590 cm^{-1} were assigned to the D and G bands of graphene, respectively [54, 55].

The surface area and porous structure of B-TiO_{2-x}/G aerogel were analyzed (Fig. 3(e)). The nitrogen sorption isotherms show the type IV behavior with obvious hysteresis loop, suggesting a mesoporous structure. Moreover, a sharp N_2 uptake is presented at low pressures, indicating the existence of micropores. The specific surface area determined by Brunauer–Emmett–Teller (BET) method is 163.8 $m^2·g^{-1}$. The pore size distribution was calculated from the desorption isotherm using DFT model (Fig. 3(f)), showing the presence of rich micropores and mesopores ranged from 0.5 to 5 nm with a sharp peak at ~ 0.85 nm. The existence of a large number of micropores may ascribe to the introduction of B-TiO_{2-x} nanosheets and the assembly of graphene sheets during the freeze-drying process. Moreover, the average size of micropores (0.85 nm) is larger than that of Li^+ ions, thus can facilitate the ion diffusion in the pores. Such large specific surface and porous structure are expected to increase the electrode/electrolyte contact area and shorten the ionic pathway, enhancing the electrochemical performance of B-TiO_{2-x}/G aerogel anode in the LICs.

Before constructing a LIC, the lithium-storage performance of B-TiO_{2-x}/G aerogel electrode was firstly examined in a Li half-cell within a potential window ranged from 0.01 to 3.0 V (Fig. 4). Figure 4(a) displays the CV curves of B-TiO_{2-x}/G aerogel electrode at different scan rates from 0.2 to 2 $mV·s^{-1}$. There are two pairs of redox peaks in the CV curves, indicating the reversible process of lithiation and delithiation within B-TiO_{2-x}/G aerogel. The pair of cathodic/anodic peaks at 1.8–1.6 V was contributed by the B-TiO_{2-x} crystal phase [56], and another pair of cathodic/anodic peaks at around 2.1/1.7 V is attributed to the insertion and removal of Li^+ into and out of anatase TiO_2. The contributions from surface capacitive effects and diffusion-controlled insertion processes can be quantitatively separated by $i = k_1v + k_2v^{1/2}$, where i is the current (A), v is the sweep rate ($mV·s^{-1}$), and k_1 and k_2 are adjustable values [38]. Figure 4(b) clearly reveals a linear correlation between the peak currents and the scan rates, indicating the kinetics are majorly surface-controlled.

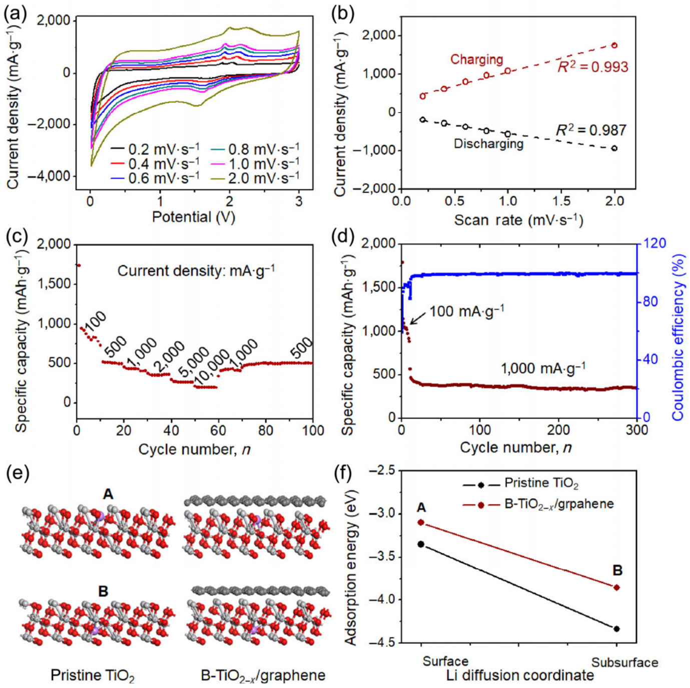

Figure 4 (a) CV curves of B-TiO_{2-x}/G aerogel electrode in a Li half-cell at various scan rates. (b) Corresponding correlations between the charge–discharge peak current densities and scan rates. (c) Rate performance of B-TiO_{2-x}/G aerogel electrode at different current densities. (d) Cycling performance of B-TiO_{2-x}/G aerogel electrode at 1,000 $mA·g^{-1}$. (e) DFT calculation of optimized Li^+ storage sites in the Li^+ diffusion paths of pristine TiO_2 and B-TiO_{2-x}/G aerogel. (f) Corresponding calculated Li^+ adsorption energies of the Li^+ storage sites in (e).

Figure 4(c) shows the rate capability of B-TiO_{2-x}/G aerogel electrode. The B-TiO_{2-x}/G aerogel electrode delivers discharge capacities of 732.7, 457.0, 373.3, 296.0, 261.4 and 193.9 $mAh·g^{-1}$ at the current densities of 100, 500, 1,000, 2,000, 5,000 and 10,000 $mA·g^{-1}$, respectively, illustrating its excellent rate capability. In contrast, for the control sample of pristine graphene aerogel without the addition of B-TiO_{2-x} nanosheets, the reversible discharge capacities are 520.8, 324.7, 243.7, 195.2, 140.8 and 114.3 $mAh·g^{-1}$ at these current densities (Fig. S2 in the ESM), respectively. The specific capacities of B-TiO_{2-x}/G aerogel are much better than those of pristine graphene aerogel, indicating that the electrochemical performance is greatly enhanced by the incorporation of B-TiO_{2-x} nanosheets. Moreover, the B-TiO_{2-x}/G aerogel electrode also displays promising durability (Fig. 4(d)). After activated at 100 $mA·g^{-1}$ for 10 cycles, the B-TiO_{2-x}/G aerogel electrode shows remarkable cycling stability at high current density, maintaining a high reversible capacity of 342.5 $mAh·g^{-1}$ after 300 cycles at 1,000 $mA·g^{-1}$ and a Coulombic efficiency of ~ 100%. The electrochemical impedance spectra (EIS) of the B-TiO_{2-x}/G aerogel electrode before and after cycling were tested. As shown in Fig. S3 in the ESM, the resistance after cycling is slightly higher than that before cycling. Such superior electrochemical performances can be attributed to the synergistic effect of the high ion/electron transfer properties and the highly-reversible Li^+ storage behavior of B-TiO_{2-x}/G aerogel.

In order to clarify the enhancement mechanism of electrochemical performance, the Li^+ storage behaviors in pristine TiO_2 and B-TiO_{2-x}/G aerogel were also investigated by DFT calculations (as detailed in Experimental section). As shown in Fig. 4(e), we considered two configurations of Li^+ ion adsorption, including the occupation of surface adsorption site (A) and subsurface insertion site (B). The corresponding Li^+ adsorption energies of pristine TiO_2 and B-TiO_{2-x}/G structures are plotted in Fig. 4(f). The Li^+ adsorption energies at the surface and subsurface layer of B-TiO_{2-x}/G are −3.10 and −3.85 eV, respectively, which are both higher than those of pristine TiO_2 (−3.35 and −4.33 eV, respectively). Compared with other electrode material systems, such as two-dimensional (2D) Mo_2B_2, Fe_2B_2, black phosphorene, and transition metal carbide (TiC_2) [57, 58], the Li diffusion energy barrier needs to be reduced. However, as shown in Fig. S4 in the ESM, it can also be observed that the Li^+ diffusion energy barrier of B-TiO_{2-x}/G, along the diffusion path from the subsurface insertion site (B) to the surface adsorption site (A), is smaller than that of pristine TiO_2. On the basis of the relative potential energies of Li atom at different sites, it can be concluded that the Li^+ diffusion energy barrier is affected by the introduction of graphene. This result indicates that the synergistic effect of B-TiO_2 and graphene nanosheets is conducive to the lithium storage performances.

So far, most reports about hybrid LICs have focused on the design and optimization of anode materials. However, to obtain good comprehensive performances, the exploration of cathode material is also very important. Our group has found that pine needles derived MPC with high surface area and appropriate pore size can be applied as a high-capacity cathode material for LICs [26]. The charge–discharge curves of MPC electrode under different current densities show nearly linear shapes (Fig. S5(a) in the ESM), revealing its ideal capacitive behavior within a large voltage window (up to 4.5 V). Figure S5(b) in the ESM shows the specific capacities of MPC electrode as a function of current density, indicating its good rate performance.

The electrochemical performances of integrated B-TiO_{2-x}/G aerogel||MPC LICs with $LiPF_6$-based carbonate electrolyte were systematically investigated. During the charging process, Li^+ cations are stored in the B-TiO_{2-x}/G aerogel anode, and PF_6^- anions are absorbed into the porous structure of MPC cathode. The working potential windows of both electrodes are determined by CV analysis in Li half cells (Fig. 4(a)). To avoid the risk of electrolyte decomposition and side reactions, the working potential window of the hybrid LICs was set between 1.0–4.0 V (Fig. 5(a)), which is much higher than that of commercial supercapacitors with organic electrolytes (normally 0–2.7 V) [59]. Such a large voltage window would greatly contribute to the energy density of LICs. The galvanostatic charge–discharge curves of B-TiO_{2-x}/G aerogel||MPC LICs at different current densities from 200 to 5,000 $mA{\cdot}g^{-1}$ are shown in Fig. 5(b). The shapes of charge–discharge curves are different from the typical triangular profiles of symmetric carbon-based supercapacitors, suggesting that the Li^+ storage in the hybrid LICs was based on the combination of battery-type Li-intercalation and EDLC-type mechanisms. On the basis of the discharging curves, C_s of the hybrid LIC was calculated to be 332.8 $F{\cdot}g^{-1}$ at 200 $mA{\cdot}g^{-1}$. The value of C_s could still maintain at ~ 128.8 $F{\cdot}g^{-1}$ even at the high current density of 5,000 $mA{\cdot}g^{-1}$ (Fig. 5(c)).

To further compare the device performances, the Ragone plot of the B-TiO_{2-x}/G aerogel||MPC LIC and other previously reported high-performance LICs are shown in Fig. 5(d). The energy density and power density of the hybrid LIC based on the total mass of active materials can be calculated by the Eqs. (2)–(4) in Experimental section. A high energy density of 166.4 $Wh{\cdot}kg^{-1}$ could be achieved at a power density of 492 $W{\cdot}kg^{-1}$, and it also delivered about 17.1 $Wh{\cdot}kg^{-1}$ at a high power output of 7.9 $kW{\cdot}kg^{-1}$. The energy and power density of the present LIC is higher than previously reported TiO_2-based LICs devices. Compared with other high-performance hybrid LICs, the hybrid LIC in this work also shows relatively high energy density and power density (see Table S1 in the ESM) [5, 15, 16, 27–38]. The cycle stability is also an important parameter to evaluate the electrochemical performance of LICs. Encouragingly, the B-TiO_{2-x}/G aerogel||MPC LIC exhibits a stable cycle performance for 3,000 cycles at current density of 2,000 $mA{\cdot}g^{-1}$, showing a ~ 87% retention of its initial capacitance and high Coulomic efficiency (Fig. 5(e)). To demonstrate the potential application of the as-prepared B-TiO_{2-x}/G aerogel||MPC LIC, a light-emitting diode (LED) panel consisting of 34 LEDs with a pattern of "NJU" logo was powered by a single LIC device after fast charging, as shown in the inset in Fig. 5(e).

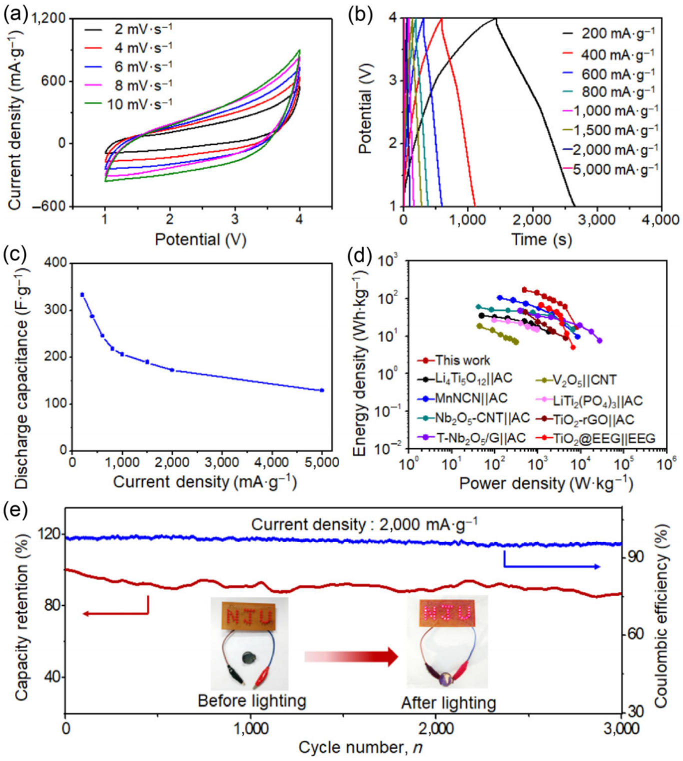

Figure 5 (a) CV curves of B-TiO_{2-x}/G aerogel||MPC LICs within the potential window of 1.0–4.0 V. (b) Charge–discharge curves of B-TiO_{2-x}/G aerogel||MPC LICs at different current densities. (c) Specific discharge capacities of B-TiO_{2-x}/G aerogel||MPC LICs at different current densities (100–5,000 $mA{\cdot}g^{-1}$). (d) Ragone plots of B-TiO_{2-x}/G aerogel||MPC LICs in this work compared with other LICs in previous reports [5, 15, 16, 27–38]. (e) Cycle performance and Coulombic efficiency of B-TiO_{2-x}/G aerogel||MPC LICs at a large current density of 2,000 $mA{\cdot}g^{-1}$ The inset shows the optical images of a LED panel powered by a single B-TiO_{2-x}/G aerogel||MPC LIC.

4 Conclusion

In summary, this work demonstrates the 3D-hieretchical B-TiO_{2-x}/G aerogel with fast kinetics can be employed as the anode of high-performance LICs. The B-TiO_{2-x}/G aerogel prepared by a facile hydrothermal approach delivers very high reversible capacity and excellent rate capability. The designed LICs show outstanding electrochemical performance, which can be due to the following reasons: (1) The large surface area and short diffusion length originated from the 3D hierarchical porous structure; (2) the high electrical conductivity, enhanced diffusion kinetics, and fast electron/ion transport pathways resulted from the oxygen vacancies and graphene conductive network; (3) the well-matched B-TiO_{2-x}/G aerogel anode and MPC cathode can improve the kinetics imbalance in LICs. The maximum energy densities of 166.4 $Wh{\cdot}kg^{-1}$ can be achieved at 492 $W{\cdot}kg^{-1}$. Still, energy densities of 17.1 $Wh{\cdot}kg^{-1}$ can be maintained at high power densities of 7.9 $kW{\cdot}kg^{-1}$. We hope this strategy of combined anode and cathode material design can bring new insights for designing high-performance hybrid capacitors.

Acknowledgements

This work was supported by the National Key R&D Program of China (Nos. 2017YFA0208200, 2016YFB0700600, and 2015CB659300), the National Natural Science Foundation of China (Nos. 21872069, 51761135104, and 21573108), Natural Science Foundation of Jiangsu Province (Nos. BK20180008 and BK20150583), High-Level Entrepreneurial and Innovative Talents Program of Jiangsu Province, and the Fundamental Research Funds for the Central Universities.

Electronic Supplementary Material: Supplementary material (Table S1 and Figs. S1–S5) is available in the online version of this article at https://doi.org/10.1007/s12274-019-2427-3.

References

[1] Amatucci, G. G.; Badway, F.; Du Pasquier, A.; Zheng, T. An asymmetric hybrid nonaqueous energy storage cell. *J. Electrochem. Soc.* **2001**, *148*, A930–A939.

[2] Ma, Y. F.; Chang, H. C.; Zhang, M.; Chen, Y. S. Graphene-based materials for lithium-ion hybrid supercapacitors. *Adv. Mater.* **2015**, *27*, 5296–5308.

[3] Dong, S. Y.; Li, H. S.; Wang, J. J.; Zhang, X. G.; Ji, X. L. Improved flexible Li-ion hybrid capacitors: Techniques for superior stability. *Nano Res.* **2017**, *10*, 4448–4456.

[4] Aravindan, V.; Lee, Y. S.; Madhavi, S. Best practices for mitigating irreversible capacity loss of negative electrodes in Li-ion batteries. *Adv. Energy Mater.* **2017**, *7*, 1602607.

[5] Aravindan, V.; Cheah, Y. L.; Mak, W. F.; Wee, G.; Chowdari, B. V. R.; Madhavi, S. Fabrication of high energy-density hybrid supercapacitors using electrospun V_2O_5 nanofibers with a self-supported carbon nanotube network. *ChemPlusChem* **2012**, *77*, 570–575.

[6] Ding, J.; Wang, H. L.; Li, Z.; Cui, K.; Karpuzov, D.; Tan X. H.; Kohandehghan, A.; Mitlin, D. Peanut shell hybrid sodium ion capacitor with extreme energy–power rivals lithium ion capacitors. *Energy Environ. Sci.* **2015**, *8*, 941–955.

[7] Jiang, H.; Hu, Y. J.; Guo, S. J.; Yan, C. Y.; Lee, P. S.; Li, C. Z. Rational design of MnO/carbon nanopeapods with internal void space for high-rate and long-life Li-ion batteries. *ACS Nano* **2014**, *8*, 6038–6046.

[8] Wang, H. W.; Zhu, C. R.; Chao, D. L.; Yan, Q. Y.; Fan, H. J. Nonaqueous hybrid lithium-ion and sodium-ion capacitors. *Adv. Mater.* **2017**, *29*, 1702093.

[9] Wang, H. W.; Zhang, Y.; Ang, H. X.; Zhang, Y. Q.; Tan, H. T.; Zhang, Y. F.; Guo, Y. Y.; Franklin, J. B.; Wu, X. L.; Srinivasan, M. et al. A high-energy lithium-ion capacitor by integration of a 3D interconnected titanium carbide nanoparticle chain anode with a pyridine-derived porous nitrogen-doped carbon cathode. *Adv. Funct. Mater.* **2016**, *26*, 3082–3093.

[10] Suryawanshi, A.; Aravindan, V.; Mhamane, D.; Yadav, P.; Patil, S.; Madhavi, S.; Ogale, S. Excellent performance of Fe_3O_4-perforated graphene composite as promising anode in practical Li-ion configuration with $LiMn_2O_4$. *Energy Storage Mater.* **2015**, *1*, 152–157.

[11] Zhang, S. J.; Li, C.; Zhang, X.; Sun, X. Z.; Wang, K.; Ma, Y. W. High performance lithium-ion hybrid capacitors employing Fe_3O_4–graphene composite anode and activated carbon cathode. *ACS Appl. Mater. Interfaces* **2017**, *9*, 17136–17144.

[12] Wang, H. L.; Xu, Z. W.; Li, Z.; Cui, K.; Ding, J.; Kohandehghan, A.; Tan, X. H.; Zahiri, B.; Olsen, B. C.; Holt, C. M. B. et al. Hybrid device employing three-dimensional arrays of MnO in carbon nanosheets bridges battery-supercapacitor divide. *Nano Lett.* **2014**, *14*, 1987–1994.

[13] Yang, M.; Zhong, Y. R.; Ren, J. J.; Zhou, X. L.; Wei, J. P.; Zhou, Z. Fabrication of high-power Li-ion hybrid supercapacitors by enhancing the exterior surface charge storage. *Adv. Energy Mater.* **2015**, *5*, 1500550.

[14] Wang, H. W.; Guan, C.; Wang, X. F.; Fan, H. J. A high energy and power Li-ion capacitor based on a TiO_2 nanobelt array anode and a graphene hydrogel cathode. *Small* **2015**, *11*, 1470–1477.

[15] Tang, G.; Cao, L. J.; Xiao, P.; Zhang, Y. H.; Liu, H. A novel high energy hybrid Li-ion capacitor with a three-dimensional hierarchical ternary nanostructure of hydrogen-treated TiO_2 nanoparticles/conductive polymer/carbon nanotubes anode and an activated carbon cathode. *J. Power Sources* **2017**, *355*, 1–7.

[16] Kong, L. P.; Zhang, C. F.; Wang, J. T.; Qiao, W. M.; Ling, L. C.; Long, D. H. Free-standing T-Nb_2O_5/graphene composite papers with ultrahigh gravimetric/volumetric capacitance for Li-ion intercalation pseudocapacitor. *ACS Nano* **2015**, *9*, 11200–11208.

[17] Song, M. Y.; Kim, N. R.; Yoon, H. J.; Cho, S. Y.; Jin, H. J.; Yun, Y. S. Long-lasting Nb_2O_5-based nanocomposite materials for Li-ion storage. *ACS Appl. Mater. Interfaces* **2017**, *9*, 2267–2274.

[18] Li, T. Q.; Beidaghi, M.; Xiao, X.; Huang, L.; Hu, Z. M.; Sun, W. M.; Chen, X.; Gogotsi, Y.; Zhou, J. Ethanol reduced molybdenum trioxide for Li-ion capacitors. *Nano Energy* **2016**, *26*, 100–107.

[19] Liu, W. W.; Li, J. D.; Feng, K.; Sy, A.; Liu, Y. S.; Lim, L.; Lui, G.; Tjandra, R.; Rasenthiram, L.; Chiu, G. et al. Advanced Li-ion hybrid supercapacitors based on 3D graphene–foam composites. *ACS Appl. Mater. Interfaces* **2016**, *8*, 25941–25953.

[20] Yang, C.; Lan, J. L.; Liu, W. X.; Liu, Y.; Yu, Y. H.; Yang, X. P. High-performance Li-ion capacitor based on an activated carbon cathode and well-dispersed ultrafine TiO_2 nanoparticles embedded in mesoporous carbon nanofibers anode. *ACS Appl. Mater. Interfaces* **2017**, *9*, 18710–18719.

[21] Yang, S. B.; Feng, X. L.; Müllen, K. Sandwich-like, graphene-based titania nanosheets with high surface area for fast lithium storage. *Adv. Mater.* **2011**, *23*, 3575–3579.

[22] Myung, S. T.; Kikuchi, M.; Yoon, C. S.; Yashiro, H.; Kim, S. J.; Sun, Y. K.; Scrosati, B. Black anatase titania enabling ultra high cycling rates for rechargeable lithium batteries. *Energy Environ. Sci.* **2013**, *6*, 2609–2614.

[23] Guan, D. D.; Yu, Q.; Xu, C.; Tang, C. J.; Zhou, L.; Zhao, D. Y.; Mai, L. Q. Aerosol synthesis of trivalent titanium doped titania/carbon composite microspheres with superior sodium storage performance. *Nano Res.* **2017**, *10*, 4351–4359.

[24] Li, N.; Liu, G.; Zhen, C.; Li, F.; Zhang, L. L.; Cheng, H. M. Battery performance and photocatalytic activity of mesoporous anatase TiO_2 nanospheres/graphene composites by template-free self-assembly. *Adv. Funct. Mater.* **2011**, *21*, 1717–1722.

[25] Liu, H.; Li, W.; Shen, D. K.; Zhao, D. Y.; Wang, G. X. Graphitic carbon conformal coating of mesoporous TiO_2 hollow spheres for high-performance lithium ion battery anodes. *J. Am. Chem. Soc.* **2015**, *137*, 13161–13166.

[26] Zhu, G. Y.; Chen, T.; Wang, L.; Ma, L. B.; Hu, Y.; Chen, R. P.; Wang, Y. R.; Wang, C. X.; Yan, W.; Tie, Z. X. et al. High energy density hybrid lithium-ion capacitor enabled by Co_3ZnC@N-doped carbon nanopolyhedra anode and microporous carbon cathode. *Energy Storage Mater.* **2018**, *14*, 246–252.

[27] Kim, H.; Cho, M. Y.; Kim, M. H.; Park, K. Y.; Gwon, H.; Lee, Y.; Roh, K. C.; Kang, K. A novel high-energy hybrid supercapacitor with an anatase TiO_2–reduced graphene oxide anode and an activated carbon cathode. *Adv. Energy Mater.* **2013**, *3*, 1500–1506.

[28] Wang, F. X.; Wang, C.; Zhao, Y. J.; Liu, Z. C.; Chang, Z.; Fu, L. J.; Zhu, Y. S.; Wu, Y. P.; Zhao, D. Y. A quasi-solid-state Li-ion capacitor based on porous TiO_2 hollow microspheres wrapped with graphene nanosheets. *Small* **2016**, *12*, 6207–6213.

[29] Aravindan, V.; Shubha, N.; Ling, W. C.; Madhavi, S. Constructing high energy density non-aqueous Li-ion capacitors using monoclinic TiO_2-B nanorods as insertion host. *J. Mater. Chem. A* **2013**, *1*, 6145–6151.

[30] Wang, G.; Liu, Z. Y.; Wu, J. N.; Lu, Q. Preparation and electrochemical capacitance behavior of TiO_2-B nanotubes for hybrid supercapacitor. *Mater. Lett.* **2012**, *71*, 120–122.

[31] Jung, H. G.; Venugopal, N.; Scrosati, B.; Sun, Y. K. A high energy and power density hybrid supercapacitor based on an advanced carbon-coated $Li_4Ti_5O_{12}$ electrode. *J. Power Sources* **2013**, *221*, 266–271.

[32] Liu, C. F.; Zhang, C. K.; Fu, H. Y.; Nan, X. H.; Cao, G. Z. Exploiting high-performance anode through tuning the character of chemical bonds for Li-ion batteries and capacitors. *Adv. Energy Mater.* **2017**, *7*, 1601127.

[33] Wang, X. L.; Li, G.; Tjandra, R.; Fan, X. Y.; Xiao, X. C.; Yu, A. P. Fast lithium-ion storage of Nb_2O_5 nanocrystals *in situ* grown on carbon nanotubes for high-performance asymmetric supercapacitors. *RSC Adv.* **2015**, *5*, 41179–41185.

[34] Lim, E.; Jo, C.; Kim, H.; Kim, M. H.; Mun, Y.; Chun, J.; Ye, Y.; Hwang, J.; Ha, K. S.; Roh, K. C. et al. Facile synthesis of Nb_2O_5@carbon core–shell nanocrystals with controlled crystalline structure for high-power anodes in hybrid supercapacitors. *ACS Nano* **2015**, *9*, 7497–7505.

[35] Luo, J. Y.; Xia, Y. Y. Electrochemical profile of an asymmetric supercapacitor using carbon-coated $LiTi_2(PO_4)_3$ and active carbon electrodes. *J. Power Sources* **2009**, *186*, 224–227.

[36] Du, H. P.; Yang, H.; Huang, C. S.; He, J. J.; Liu, H. B.; Li, Y. L. Graphdiyne applied for lithium-ion capacitors displaying high power and energy densities. *Nano Energy* **2016**, *22*, 615–622.

[37] Que, L. F.; Yu, F. D.; Wang, Z. B.; Gu, D. M. Pseudocapacitance of TiO_{2-x}/CNT anodes for high-performance quasi-solid-state Li-ion and

Na-ion capacitors. *Small* **2018**, *14*, 1704508.

[38] Huang, H. J.; Wang, X.; Tervoort, E.; Zeng, G. B.; Liu, T.; Chen, X.; Sologubenko, A.; Niederberger, M. Nano-sized structurally disordered metal oxide composite aerogels as high-power anodes in hybrid supercapacitors. *ACS Nano* **2018**, *12*, 2753–2763.

[39] Ma, L. B.; Gao, X.; Zhang, W. J.; Yuan, H.; Hu, Y.; Zhu, G. Y.; Chen, R. P.; Chen, T.; Tie, Z. X.; Liu, J. et al. Ultrahigh rate capability and ultralong cycling stability of sodium-ion batteries enabled by wrinkled black titania nanosheets with abundant oxygen vacancies. *Nano Energy* **2018**, *53*, 91–96.

[40] Kresse, G.; Furthmüller, J. Efficiency of *ab-initio* total energy calculations for metals and semiconductors using a plane-wave basis set. *Comput. Mater. Sci.* **1996**, *6*, 15–50.

[41] Kresse, G.; Hafner, J. *Ab initio* molecular dynamics for liquid metals. *Phys. Rev. B* **1993**, *47*, 558–561.

[42] Kresse, G.; Hafner, J. *Ab initio* molecular-dynamics simulation of the liquid-metal–amorphous-semiconductor transition in germanium. *Phys. Rev. B* **1994**, *49*, 14251–14269.

[43] Kresse, G.; Furthmüller, J. Efficient iterative schemes for *ab initio* total-energy calculations using a plane-wave basis set. *Phys. Rev. B* **1996**, *54*, 11169–11186.

[44] Perdew, J. P.; Burke, K.; Ernzerhof M. Generalized gradient approximation made simple. *Phys. Rev. Lett.* **1996**, *77*, 3865–3868.

[45] Monkhorst, H. J.; Pack, J. D. Special points for brillouin-zone integrations. *Phys. Rev. B* **1976**, *13*, 5188–5192.

[46] Grimme, S. Semiempirical GGA-type density functional constructed with a long-range dispersion correction. *J. Comput. Chem.* **2006**, *27*, 1787–1799.

[47] Grimme, S.; Antony, J.; Ehrlich, S.; Krieg, H. A consistent and accurate *ab initio* parametrization of density functional dispersion correction (DFT-D) for the 94 elements H-Pu. *J. Chem. Phys.* **2010**, *132*, 154104.

[48] Hummers, W. S. Jr.; Offeman, R. E. Preparation of graphitic oxide. *J. Am. Chem. Soc.* **1958**, *80*, 1339.

[49] Myung, S. T.; Takahashi, N.; Komaba, S.; Yoon, C. S.; Sun, Y. K.; Amine, K.; Yashiro, H. Nanostructured TiO_2 and its application in lithium-ion storage. *Adv. Funct. Mater.* **2011**, *21*, 3231−3241.

[50] Tan, H. Q.; Zhao, Z.; Niu, M.; Mao, C. Y.; Cao, D. P.; Cheng, D. J.; Feng, P. Y.; Sun, Z. C. A facile and versatile method for preparation of colored TiO_2 with enhanced solar-driven photocatalytic activity. *Nanoscale* **2014**, *6*, 10216−10223.

[51] Zhang, Z. Y.; Xiao, F.; Guo, Y. L.; Wang, S.; Liu, Y. Q. One-pot self-assembled three-dimensional TiO_2-graphene hydrogel with improved adsorption capacities and photocatalytic and electrochemical activities. *ACS Appl. Mater. Interfaces* **2013**, *5*, 2227–2233.

[52] Zhu, G. Y.; Chen, T.; Hu, Y.; Ma, L. B.; Chen, R. P.; Lv, H. L.; Wang, Y. R.; Liang, J.; Li, X. J.; Yan, C. Z. et al. Recycling $PM_{2.5}$ carbon nanoparticles generated by diesel vehicles for supercapacitors and oxygen reduction reaction. *Nano Energy* **2017**, *33*, 229–237.

[53] Chen, J.; Ding, Z. Y.; Wang, C.; Hou, H. S.; Zhang, Y.; Wang, C. W.; Zou, G. Q.; Ji, X. B. Black anatase titania with ultrafast sodium-storage performances stimulated by oxygen vacancies. *ACS Appl. Mater. Interfaces* **2016**, *8*, 9142–9151.

[54] Zhu, Y. Q.; Cao, T.; Li, Z.; Chen, C.; Peng, Q.; Wang, D. S.; Li, Y. D. Two-dimensional SnO_2/graphene heterostructures for highly reversible electrochemical lithium storage. *Sci. China Mater.* **2018**, *61*, 1527–1535.

[55] Zhu, Y. Q.; Cao, T.; Cao, C. B.; Ma, X. L.; Xu, X. Y.; Li, Y. D. A general synthetic strategy to monolayer graphene. *Nano Res.* **2018**, *11*, 3088–3095.

[56] Wang, Y.; Su, X. W.; Lu, S. Shape-controlled synthesis of TiO_2 hollow structures and their application in lithium batteries. *J. Mater. Chem.* **2012**, *22*, 1969–1976.

[57] Guo, Z. L.; Zhou, J.; Sun, Z. M. New two-dimensional transition metal borides for Li ion batteries and electrocatalysis. *J. Mater. Chem. A* **2017**, *5*, 23530–23535.

[58] Peng, Q.; Hu, K. M.; Sa, B. S.; Zhou, J.; Wu, B.; Hou, X. H.; Sun, Z. M. Unexpected elastic isotropy in a black phosphorene/TiC_2 van der waals heterostructure with flexible Li-ion battery anode applications. *Nano Res.* **2017**, *10*, 3136–3150.

[59] Fuertes, A. B.; Sevilla, M. Hierarchical microporous/mesoporous carbon nanosheets for high-performance supercapacitors. *ACS Appl. Mater. Interfaces* **2015**, *7*, 4344–4353.